Volume 8
Number 38
14 October 2020
Pages 13095–13468

Journal of Materials Chemistry C

Materials for optical, magnetic and electronic devices

rsc.li/materials-c

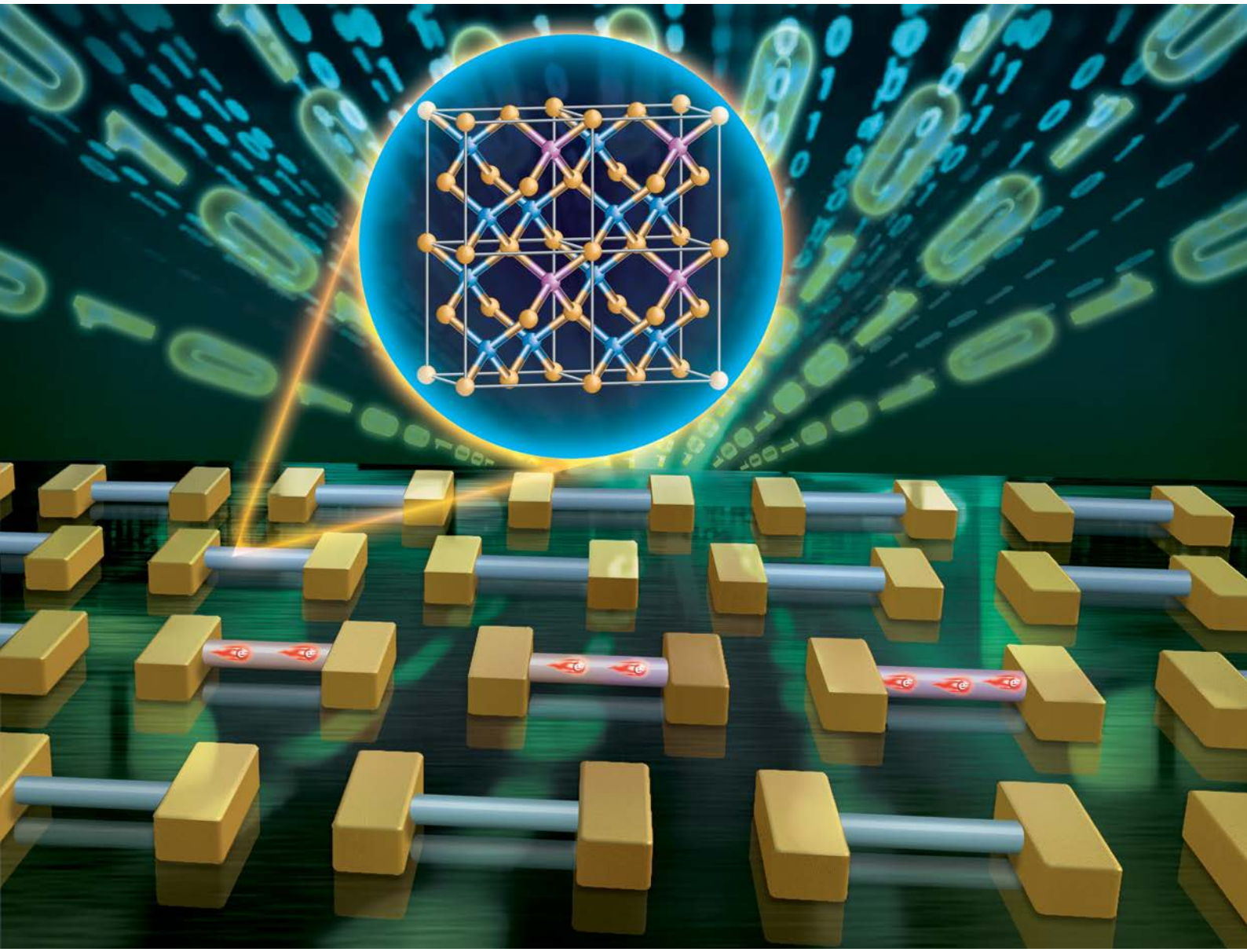

ISSN 2050-7526

ROYAL SOCIETY OF CHEMISTRY

PAPER

Johnny C. Ho *et al.*

Unusual phase-pure zinc blende and highly-crystalline As-rich $InAs_{1-x}Sb_x$ nanowires for high-mobility transistors

Journal of Materials Chemistry C

ROYAL SOCIETY OF CHEMISTRY

PAPER

View Article Online
View Journal | View Issue

Cite this: J. Mater. Chem. C, 2020, 8, 13189

Unusual phase-pure zinc blende and highly-crystalline As-rich $InAs_{1-x}Sb_x$ nanowires for high-mobility transistors†

SenPo Yip,[abcd] Dapan Li,[a] Fangzhou Li,[a] Wei Wang,[a] Xiaolin Kang,[a] You Meng,[a] Heng Zhang,[ad] Zhengxun Lai,[a] Fei Wang[ab] and Johnny C. Ho*[abcd]

Due to the excellent electrical and optical properties, small bandgap III–V nanowire (NW) materials hold great promise for future electronics and optoelectronics. In particular, $InAs_{1-x}Sb_x$, the ternary alloy of InAs and InSb, is one of the most studied III–V nanomaterial systems; however, the As-rich $InAs_{1-x}Sb_x$ NWs are usually obtained with significant crystal phase mixing and high density of planar defects, limiting their electrical transport characteristics. In this work, unusual phase-pure zinc blende and highly-crystalline As-rich $InAs_{1-x}Sb_x$ NWs with $x < 0.2$ are successfully achieved using solid-source chemical vapor deposition, and this excellent phase-purity and crystallinity has not been reported elsewhere. By simply controlling the precursor powder mixing ratio between InAs and InSb, the morphology and composition of NWs can be controlled reliably. When these $InAs_{1-x}Sb_x$ NWs are fabricated into field-effect transistors, they exhibit a superior device performance, especially a high electron mobility. Specifically, the average peak mobility of the $InAs_{0.948}Sb_{0.052}$ NW device can be improved up to 3160 $cm^2\ V^{-1}\ s^{-1}$, which is substantially better than that of the pure InAs NW counterparts (2030 $cm^2\ V^{-1}\ s^{-1}$). This mobility enhancement can be attributed to the Sb-alloyed-induced electron effective mass reduction. Also, there exists a surface charge accumulation layer on the NWs as confirmed by the decrease of device transconductance measured under vacuum, indicating future possibilities to manipulate the NW surface for enhanced functionality. All these results evidently indicate the potential of these phase-pure zinc blende As-rich $InAs_{1-x}Sb_x$ NWs for high-mobility devices.

Received 7th June 2020,
Accepted 29th June 2020

DOI: 10.1039/d0tc02715d

rsc.li/materials-c

Introduction

In the past decades, due to the intriguing properties such as direct bandgap and high carrier mobility, small bandgap III–V materials, including InAs (E_g = 0.35 eV), InSb (0.17 eV), GaSb (0.726 eV) and also their alloys, have been widely considered as promising active materials for high-speed electronics,[1,2] photodetectors,[3–5] lasers,[6,7] gas detectors[8–10] and so on.[11] In particular, their alloy configurations would provide extra degrees of freedom for lattice engineering and bandgap tuning. Specifically, by simply adjusting the atomic ratio of As and Sb, the bandgap of $InAs_{1-x}Sb_x$ could be as low as 0.145 eV (at 0 K; x = 0.63),[12] which is the lowest bandgap energy among all III–V materials, being advantageous in enabling many advanced device applications in mid-infrared sensing,[13] LEDs[14] and lasers.[15] In addition to the benefits of their bulk form, small bandgap III–V nanowires (NWs) possess the unique characteristics of superior surface-to-volume ratio and excellent strain relaxation when building heterostructures. In this case, ternary alloy NWs (*e.g.* $InAs_{1-x}Sb_x$, $GaAs_{1-x}Sb_x$ and $In_xGa_{1-x}Sb$) have been preliminarily explored and constructed into different device structures with respectable performances.[16–20] For instance, using the kinked GaSb/GaInSb NWs as the sensing materials, Ma *et al.* demonstrated a photodetector with high responsivity ($\sim 10^3$) in the optical communication region (1550 nm).[21] Recently, by utilizing $In_xGa_{1-x}Sb$ NWs and their NW parallel arrays, our group has achieved high-mobility p-type transistors and broadband and ultrafast photodetectors with the response time down to tens of μs.[22] In any case, to date, there are still very limited detailed studies on another technologically important ternary alloy of $InAs_{1-x}Sb_x$, with more careful and systematic investigations urgently needed.

[a] Department of Materials Science and Engineering, City University of Hong Kong, Kowloon 999077, Hong Kong SAR, China. E-mail: johnnyho@cityu.edu.hk
[b] State Key Laboratory of Terahertz and Millimeter Waves, City University of Hong Kong, Kowloon 999077, Hong Kong SAR, China
[c] Centre for Functional Photonics, City University of Hong Kong, Kowloon 999077, Hong Kong SAR, China
[d] Shenzhen Research Institute, City University of Hong Kong, Shenzhen 518057, P. R. China

† Electronic supplementary information (ESI) available. See DOI: 10.1039/d0tc02715d

Generally, $InAs_{1-x}Sb_x$ NWs can be synthesized by chemical vapor deposition or molecular beam epitaxy using either Au nanoparticles as catalysts[23,24] or a catalyst-free approach.[16,25] It is well observed that when x is less than 0.13, the $InAs_{1-x}Sb_x$ NWs are usually grown with mixed phases of wurtzite (WZ) and zinc blende (ZB) together with large concentrations of twinning and stacking faults.[16,23] These planar defects are believed to act as a source of carrier scattering centres to degrade the carrier mobility.[16] In particular, Boland *et al.* reported that the mobility of a single $InAs_{0.65}Sb_{0.35}$ NW, which is free from any planar defects, can be as high as 16 000 $cm^2\ V^{-1}\ s^{-1}$ measured using terahertz and Raman spectroscopy at 10 K.[26]

In this work, highly-crystalline $InAs_{1-x}Sb_x$ NWs with different compositions ($x \leq 0.2$) are successfully fabricated using solid-source catalytic chemical vapor deposition on amorphous substrates, where this simple technique has been commonly used to obtain both binary and ternary III–V NWs of different chemical stoichiometries.[22,27,28] Importantly, despite the low Sb content in these $InAs_{1-x}Sb_x$ NWs, all the NWs are grown in the unusual phase-pure structure, without any observable phase mixing and planar defects that are always observed in other reports.[16,23] By manipulating the mixing ratio of the precursor powders, the NW composition can be varied accordingly. As the Sb content increases in the powder mixture, the long and straight NWs obtained would change to the short and tapered morphologies. This morphological evolution points out a possibility for growing pure ZB $InAs_{1-x}Sb_x$ NWs for other synthesis schemes when suitable conditions are chosen. Once configured into NW field-effect transistors (FETs), the optimal $InAs_{1-x}Sb_x$ (*i.e.* $InAs_{0.948}Sb_{0.052}$) NW devices exhibit an enhanced average electron mobility of 3160 $cm^2\ V^{-1}\ s^{-1}$ as compared to that (2030 $cm^2\ V^{-1}\ s^{-1}$) of pure InAs NW devices. Also, their device transconductance is found to decrease by ~30% under vacuum, which confirms the presence of a surface charge accumulation layer being sensitive to the ambient environment. All these findings provide valuable insights for the further development of high-quality $InAs_{1-x}Sb_x$ for next-generation high-performance devices.

Results and discussion

Morphological evolution

Here, the growth of $InAs_{1-x}Sb_x$ NWs is performed in a horizontal tube furnace with different precursor powder mixing ratios (by weight) of InAs and InSb, namely, 30 : 1, 20 : 1, 10 : 1, 1 : 1 and 1 : 4. Pure InAs NWs are as well grown as the control sample (Fig. 1a). It is noted that another set of crucibles is utilized for the growth of pure InAs NWs in order to prevent the contamination from residual Sb that remains in the crucibles.[29] At first, the NW morphologies were evaluated using SEM. Based on the SEM images (Fig. 1), the pure InAs NWs exhibit a smooth morphology without any significant tapering, whereas the NWs are longer than 10 μm. When a small amount of InSb powder is added into the precursor mixture (for the cases of InAs : InSb ratios equal to 30 : 1 and 20 : 1), the NW morphology is mostly maintained with a length larger than 10 μm and a smooth surface. Approximately, these "low-Sb" $InAs_{1-x}Sb_x$ NWs are observed to have the similar diameter as compared with that of pure InAs. A more detailed diameter analysis will be discussed later. However, when an additional amount of InSb powder is added to the mixture (for the cases of an InAs : InSb ratio smaller than 10 : 1), the NWs become much thicker, and start to have a significant over-coating. As soon as the mixing ratio is larger than 1 : 1, obvious tapering

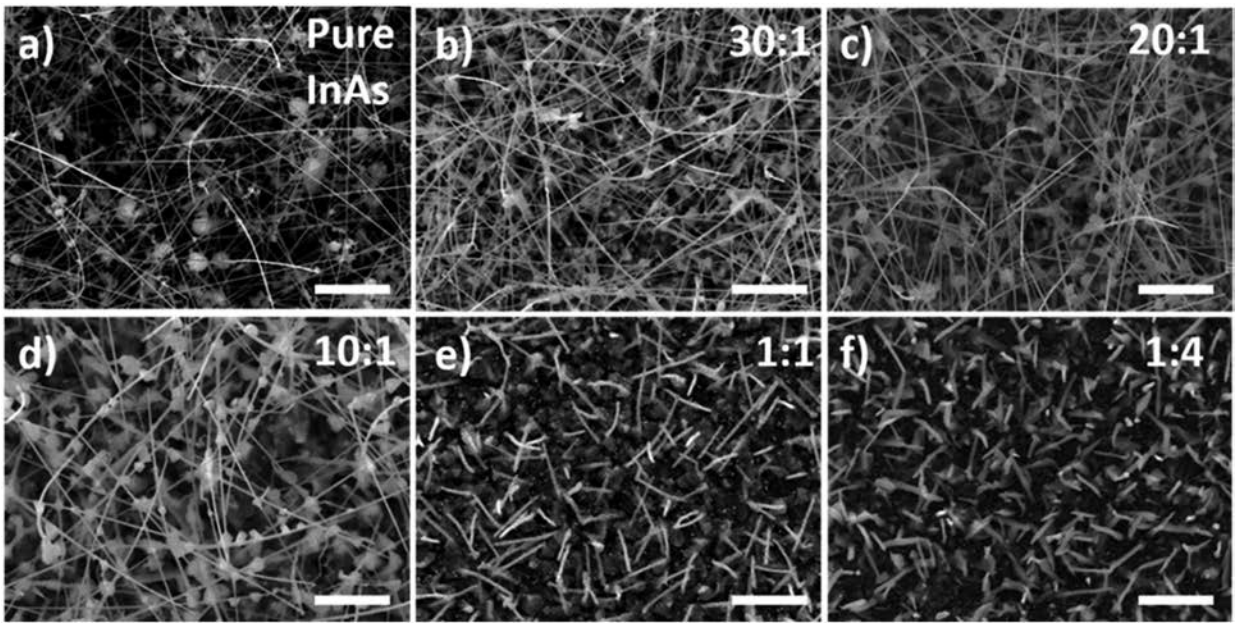

Fig. 1 SEM images of the as-grown $InAs_{1-x}Sb_x$ NWs with different precursor powder mixing ratios (by weight) of InAs : InSb: (a) pure InAs, (b) 30 : 1, (c) 20 : 1, (d) 10 : 1, (e) 1 : 1 and (f) 1 : 4. All the scale bars are 2 μm.

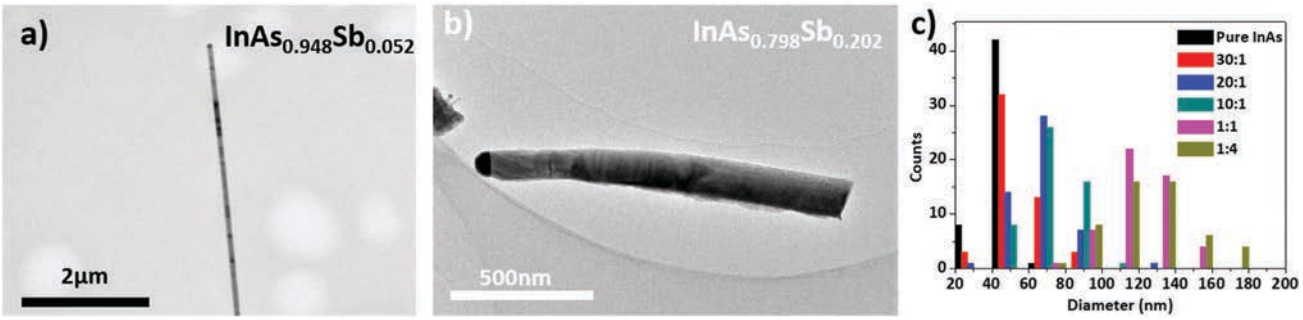

Fig. 2 TEM images of (a) $InAs_{0.948}Sb_{0.052}$ and (b) $InAs_{0.798}Sb_{0.202}$ NWs. (c) Diameter statistics of the $InAs_{1-x}Sb_x$ NWs with different compositions. The NWs grown with the powder mixing ratios of InAs : InSb = 30 : 1 and 1 : 4 are determined to have the composition of $InAs_{0.948}Sb_{0.052}$ and $InAs_{0.798}Sb_{0.202}$, respectively, from the subsequent EDS analysis.

(*i.e.* non-uniform diameter along the NW axial direction) would occur in these thick "rich-Sb" $InAs_{1-x}Sb_x$ NWs with the length greatly reduced to below 2 μm. The morphological differences between these "low-Sb" and "rich-Sb" NWs are clearly displayed in the TEM images (Fig. 2a and b). Based on the statistics of more than 50 individual NWs in each sample group, the diameter distribution of different $InAs_{1-x}Sb_x$ NWs can be assessed from the TEM images and illustrated in Fig. 2c. It is evident that the InAs and "low-Sb" $InAs_{1-x}Sb_x$ NWs are relatively thin with a narrow diameter distribution. The InAs and $InAs_{1-x}Sb_x$ NWs grown with the powder mixing ratio of InAs : InSb = 30 : 1 have the diameter of 45.7 ± 7.4 nm and 55.7 ± 13.2 nm, respectively. For the increasing Sb content, the "rich-Sb" $InAs_{1-x}Sb_x$ NWs would get thicker with a much boarder diameter distribution. The diameter of the $InAs_{1-x}Sb_x$ NWs grown with the powder mixing ratio of InAs : InSb = 1 : 4 would change to 121.6 ± 23.4 nm. The average diameter of each NW composition is also presented in Table 1. Such dramatic changes in the NW morphology and diameter are believed to be associated with the following factors. Firstly, these changes can be attributed to the enriched In absorption in the catalytic seeds during the NW growth with the increasing Sb content. In Borg's report, the increase in the x value of $InAs_{1-x}Sb_x$ NWs would increase the NW diameter.[24] This indicates that a higher Sb source vapor concentration induces larger amounts of In to be absorbed into the catalytic particles for the larger catalyst size and, subsequently, the obtained NW diameter. Secondly, the surfactant effect of Sb would also come to play an important role here as Sb is known to be a good surfactant to modify the kinetics of surface atoms during the material growth.[29,30] In fact, as reported in the literature, the Sb atoms are found to affect the axial and radial growth rate of NWs by (i) flattening the catalyst particles due to their surfactant effect in order to suppress the growth[25,31] and (ii) enhancing the group-III adatom adsorption on the NW sidewall such that the radial growth rate is elevated.[32] These abovementioned factors contribute to the morphological and diameter changes of $InAs_{1-x}Sb_x$ NWs, especially for the retarded NW growth with the higher Sb content. Moreover, the location of the NW growth region is found to change accordingly with the precursor powder mixing ratio. For the extreme case in which the InAs : InSb ratio is 1 : 4, the grown NWs are mostly located on the edge of the substrate that is on the closer end of the powder source side due to the rapid depletion of the In source vapor. All these results indicate the narrow process window to obtain the $InAs_{1-x}Sb_x$ NWs, particularly the "rich-Sb" NWs, with well controlled morphology.

Composition and crystal structure

At the same time, it is essential to determine the chemical composition of the obtained $InAs_{1-x}Sb_x$ NWs for each sample group. Based on the EDS analysis, the Sb content of NWs grown using each different precursor powder mixing ratio can be attained by averaging the Sb concentration (in atomic percent) of at least 6 different individual NWs (Fig. S2, ESI†). The average Sb concentration of each NW sample group is also summarized in Table 2. By simply adjusting the powder mixing ratio, the Sb concentration of $InAs_{1-x}Sb_x$ NWs can be varied from 3.6% to 20.2%. In other words, the lower powder mixing ratio of InAs : InSb (*i.e.* the more effective Sb content) would yield the $InAs_{1-x}Sb_x$ NWs with the higher Sb concentration, which potentially have different controllable electrical, optical and optoelectronic properties. However, because of the relatively low vapor pressure of Sb, though there is a drastic decrease in the amount of InAs powder used in the powder mixture, the obtained variation of Sb concentration of the NWs is still quite narrow. An aggressive reduction in the powder mixing ratio of InAs : InSb is essentially needed to achieve the higher Sb concentration of NWs, which suggests the limitation of the current growth scheme. In particular, with the increasing amount of InSb powder utilized, the overall length of the obtained $InAs_{1-x}Sb_x$ NWs becomes much shorter (Fig. 1). For the $InAs_{0.798}Sb_{0.202}$ NW growth, the amount of InSb powder used is already dominant in the powder mixture (with the mixing

Table 1 Average diameter of the $InAs_{1-x}Sb_x$ NWs with different powder mixing ratios

InAs : InSb	Pure InAs	30 : 1	20 : 1	10 : 1	1 : 1	1 : 4
Diameter (nm)	45.7 ± 7.4	55.7 ± 13.2	66.8 ± 14.5	74.8 ± 13.0	116.1 ± 15.6	121.6 ± 23.5

Table 2 The average Sb concentration (in atomic percent) of $InAs_{1-x}Sb_x$ NWs prepared using different precursor powder mixing ratios (by weight)

Powder mixing ratio (InAs : InSb)	x value (Sb concentration in atomic%)	Standard deviation
30 : 1	0.036	0.009
20 : 1	0.052	0.018
10 : 1	0.080	0.016
1 : 1	0.092	0.014
1 : 4	0.202	0.012

ratio of InAs : InSb = 1 : 4). With the fast depletion of the In source vapor, the grown $InAs_{0.798}Sb_{0.202}$ NWs are all shorter than 1 μm, where all the NWs are located on the edge of the substrate that is on the closer end of the powder source side. A further increase in the amount of InSb powder would make the growth of $InAs_{1-x}Sb_x$ NWs with $x \gg 0.2$ become challenging.

In fact, achieving a full range of the composition tunability of $InAs_{1-x}Sb_x$ NWs has still not been easy until now. For example, utilizing the vertical InAs NW stems as the growth template, Sorba and his team could achieve a full composition range of $InAs_{1-x}Sb_x$ NWs by the complicated chemical beam epitaxy process.[33,34] Other than these works, the Sb-rich $InAs_{1-x}Sb_x$ NWs with the x value between 0.7 and 0.8 were also achievable using Au nanoparticles *via* both the stem-assisted[24] or stemless growth process.[35] As compared with the self-catalyzed approach, where most of the x values are below 0.43,[26,31] the use of Au catalysts seems to be essential to attain a high Sb content of $InAs_{1-x}Sb_x$ NWs, which might be due to the lesser vulnerability of the catalyst particles to be flattened by the surfactant effect of Sb atoms. However, despite using the Au films as catalysts, the maximum Sb concentration of the grown $InAs_{1-x}Sb_x$ NWs is only about 20% in this work. We speculate that the high density of the obtained catalyst particles could be one of the obstacles here. Fig. S3 (ESI†) shows the Au nanoparticles formed after annealing the 0.5 nm-thick Au thin film. It is clear that the Au nanoparticle density is very high. In this case, after the nucleation, since each Au particle would act as an absorption centre of In, the In source gets consumed quickly. When a higher amount of Sb is involved, more In is required for the growth of $InAs_{1-x}Sb_x$ NWs. Therefore, the depletion of In would limit the vertical growth. As combined with the effect of the flattened catalyst particles discussed earlier, the slow growth rate limits the achievement of NWs with a higher Sb concentration. In the near future, increasing the In supply or reducing the catalyst particle density would be possible to further enhance the Sb content of the NWs.

Besides, the elemental distribution of $InAs_{1-x}Sb_x$ NWs is also examined using EDS mapping. Fig. 3 illustrates the scanning TEM HADAF image of a typical $InAs_{0.92}Sb_{0.08}$ NW and the corresponding chemical mapping of In, Au, As and Sb of the NW tip region. It is evident that In, As and Sb are all distributed in a uniform manner along both axial and radial directions of the NW. Notably, the hemispherical catalytic tip is clearly observed, which suggests that the NWs were grown using the typical vapor-liquid–solid mechanism. The tip mainly consists of Au, In and Sb, except for As, indicating that both In and Sb

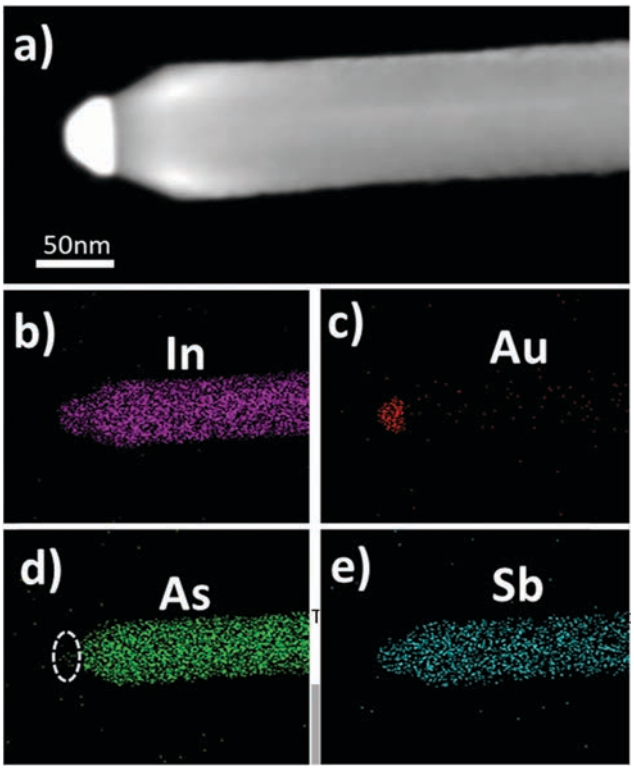

Fig. 3 (a) STEM HADAF image of a typical $InAs_{0.92}Sb_{0.08}$ NW. (b)–(e) Elemental mappings of different constituents of the NW shown in panel a. The white dotted circle indicates the insignificant concentration of As in the catalytic tip.

species are first dissolved into catalysts and precipitated to react with As in the catalyst/NW interface in order to form the NWs. This sequential reaction path of the NW growth (*i.e.* InSb to $InAs_{1-x}Sb_x$) is commonly observed in other ternary NW material synthesis.[30] A schematic description of the NW growth process is illustrated in Fig. S4 (ESI†) as well. All these results confirm the uniform distribution of the constituents within the obtained $InAs_{1-x}Sb_x$ NWs. In addition, XRD is also performed on the obtained $InAs_{1-x}Sb_x$ NWs. All the NWs exhibit the pure ZB structure without any WZ phase observed (Fig. S5, ESI†). In particular, by examining the (111) peaks located at 2θ of around 25.4°, which represent the (111) plane of ZB InAs, the peaks are found to shift towards a smaller 2θ value for the increasing Sb concentration of $InAs_{1-x}Sb_x$ NWs, indicating the increase in lattice parameter due to the larger size of Sb atoms replacing the As atoms (Fig. 4a). HRTEM is then carried out to evaluate the crystallinity of NWs. Fig. 4b–d give the HRTEM images of the representative samples of $InAs_{0.948}Sb_{0.052}$, $InAs_{0.908}Sb_{0.092}$ and $InAs_{0.798}Sb_{0.202}$ NWs. The insets show the corresponding fast Fourier transform (FFT) pattern of the NW, which points toward the NWs grown along the ⟨111⟩ direction. It should be noticed that although all three images demonstrate the growth orientation in the ⟨111⟩ direction, NWs grown in the ⟨110⟩ direction are sometimes observed (Fig. S6, ESI†); therefore, the data shown here are not decisive enough to conclude the distribution of NW growth direction. In any case, all the HRTEM images confirm the pure single-phase zinc blende

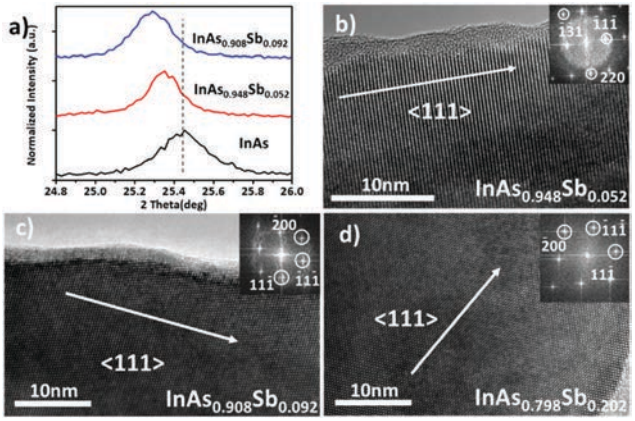

Fig. 4 (a) XRD pattern of $InAs_{1-x}Sb_x$ NWs grown with different compositions. The dashed line marks the peak position of the ZB InAs (111) plane. (b)–(d) HRTEM images of (b) $InAs_{0.948}Sb_{0.052}$, (c) $InAs_{0.908}Sb_{0.092}$ and (d) $InAs_{0.798}Sb_{0.202}$ NWs. The insets show the corresponding FFT pattern.

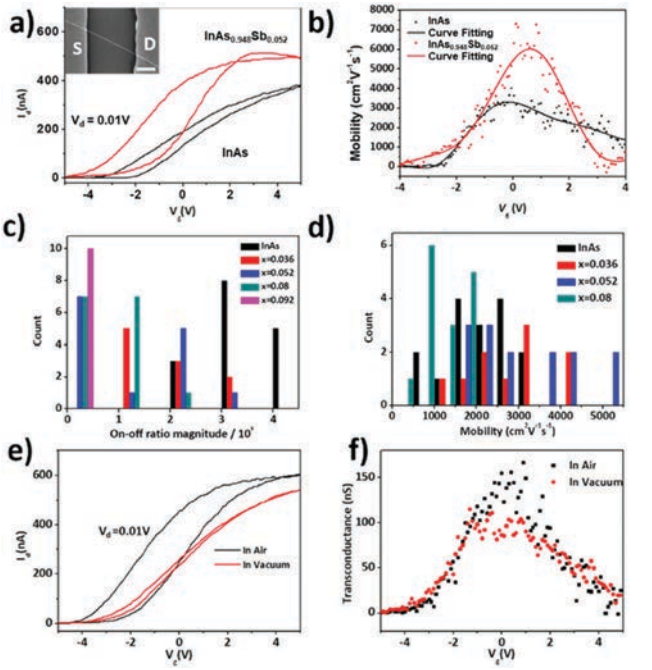

Fig. 5 (a) Transfer characteristics of typical InAs and an $InAs_{0.948}Sb_{0.052}$ NWFETs. Inset shows the top-view SEM image of an NWFET. (b) Mobility as a function of gate voltage (V_g) of the InAs and $InAs_{0.948}Sb_{0.052}$ NWFETs. The mobility values are determined based on the reverse sweep (from positive gate bias to negative gate bias) of the device transfer curves. All the peak mobility values investigated in this work are obtained by the polynomial fit of the curve. (c) On–off current ratio and (d) mobility distribution of InAs and different $InAs_{1-x}Sb_x$ NWFETs. (e) Transfer characteristics of a typical $InAs_{0.948}Sb_{0.052}$ NWFET measured in air and under vacuum, and (f) their device transconductance as a function of gate voltage during the reverse sweep.

structure over at least 30 nm of the length of the NWs. This excellent phase purity of the NWs is surprising considering that, in most of the existing reports of $InAs_{1-x}Sb_x$ NWs, when x is below 0.12, phase mixing, twinning and stacking faults are commonly observed in the NW body.[23,26] In these reports, the pure InAs NWs are usually grown in the WZ phase. However, as III-Sb NWs are more favorably grown in the ZB phase due to the low iconicity of Sb, the alloying of Sb for the growth of $InAs_{1-x}Sb_x$ NWs would easily generate phase mixing in the NW matrix and also create large amounts of stacking faults and twinning defects. When the Sb concentration keeps increasing, the ZB portions of the NWs grow at the consumption of the WZ regions along with the decrease of planar defects.[23,26] Once the Sb content hits the value of x around 0.12, the complete phase transformation of $InAs_{1-x}Sb_x$ NWs would take place, converting from the WZ phase to the ZB phase.[23,26] On the other hand, as shown in our pervious works, pure ZB InAs NWs are typically obtained using solid-source chemical vapor deposition with Au catalysts, which is also applicable in the current study.[36] Thus, it is anticipated that there is not any phase transition induced during the incorporation of Sb into the lattice matrix of ZB InAs NWs here. This finding designates the successful alloying of both InAs and InSb together into the phase-pure As-rich $InAs_{1-x}Sb_x$ NWs without any noticeable phase inversion and other planar defects.

Nanowire transistor performance

For practical applications, it is important to evaluate the electrical properties of the fabricated NWs as well as their device performance once they are configured into NW transistors. In this work, back-gated FETs are studied using individual $InAs_{1-x}Sb_x$ NWs as the device channel. As given in the transfer characteristics in Fig. 5a and Fig. S7 (ESI†), all the NW devices deliver a typical n-type semiconductor behaviour. To be specific, the $InAs_{0.948}Sb_{0.052}$ NW device can yield a higher on current but a lower on–off current ratio as compared with the InAs NW counterparts. Their output characteristics are also displayed in Fig. S8 (ESI†), where the linear relationships suggest the ohmic-like electrical contact between NW channels and metal electrodes. Using the standard square-law model, the field-effect mobility of NW devices can be assessed using the following analytical equation:

$$\mu = g_m L^2 / C_{ox} V_{DS}$$

where μ is the electrical mobility, g_m is the transconductance that is defined as dI_{DS}/dV_{GS}, L is the channel length, C_{ox} is the capacitance (see Fig. S9, ESI† for the calculation of the C_{ox} value) and V_{DS} is the drain voltage. The peak mobility of the reverse I_d–V_g sweep of representative InAs and $InAs_{0.948}Sb_{0.052}$ NWFETs is then found to be 3000 $cm^2\ V^{-1}\ s^{-1}$ and about 6000 $cm^2\ V^{-1}\ s^{-1}$, respectively (Fig. 5b). Importantly, the effect of NW composition on the device performance is also investigated. Although the average Sb concentration of NW is varied in a relatively narrow range between 0% and 20.2%, the stoichiometric dependence of the on–off current ratio and mobility of the device is obvious. With increasing Sb concentration, the on–off current ratio of the NW devices is observed to decrease, while their mobility values first increase and then decrease accordingly (Fig. 5c and d). Such a drastic decrease in the on–off current ratio would probably come from the bandgap reduction

originating from the increase of Sb content. This bandgap lowering increases the leakage current and hence lowering the on–off current ratio. On the other hand, the change of the Sb concentration also affects the average peak field-effect mobility. Here, we observe the existence of hysteresis during the I_d–V_g sweep, which makes the mobility values extracted from both forward and reverse I_d–V_g sweeps deviate. In this way, for the mobility comparison, the peak mobility of an NWFET is taken as the average value of the peak mobility extracted from both forward and reverse sweeps. The average peak mobility of an NW device with a particular composition is the average mobility of about 10–15 NWFETs. In our estimation, the average peak mobility is enhanced from 2030 $cm^2 V^{-1} s^{-1}$ of InAs NWFETs to 2800 $cm^2 V^{-1} s^{-1}$ of $InAs_{0.964}Sb_{0.036}$ NWFETs, and eventually reaches the maximum value of 3160 $cm^2 V^{-1} s^{-1}$ of $InAs_{0.948}Sb_{0.052}$ NWFETs. This increased mobility can be attributed to the Sb-alloyed-induced electron effective mass reduction.[26,37] In bulk $InAs_{1-x}Sb_x$, the effective mass of the electron is actually determined to continuously decrease as the Sb content increases up until $x = 0.6$.[38] With a lower effective mass of electron, a higher drift velocity occurred for the improved electron mobility. Notably, our peak mobility values are already higher than other reports with the similar chemical composition of $InAs_{1-x}Sb_x$ NWs, which is possibly associated with the better NW crystallinity and phase purity obtained in this work.[16,39] However, when the Sb content is increased more than 5.2 atomic percent, the average peak mobility of NWFETs starts to decline, which drops to about 1150 $cm^2 V^{-1} s^{-1}$, owing to the increasing NW diameter. These thicker NWs would inevitably degrade the gate-coupling efficiency, especially for the back-gated device configuration, deteriorating the device performance. In the future, top- and wrap-gated device configuration can be adopted to explore the high-mobility FETs using Sb-rich $InAs_{1-x}Sb_x$ NW channels.

Furthermore, the device performance of 7 different $InAs_{0.948}Sb_{0.052}$ NWFETs was also evaluated with the electrical measurement under vacuum. We then compare their performance obtained between ambient and vacuum conditions. It is noted that during the vacuum measurement, the chamber is pumped down to 5×10^{-6} Torr and maintained overnight to ensure the complete desorption of gas molecules from the NW surface. Fig. 5e shows the transfer characteristics of a representative $InAs_{0.948}Sb_{0.052}$ NWFET measured in both ambient and vacuum conditions. It is witnessed that the hysteresis of the current *versus* voltage curve (*i.e.* I_d–V_g loop) becomes a lot smaller with a comparable on–off current ratio, which can be attributed to the desorption of adsorbed gas molecules away from the NW surface during vacuum pumping. At the same time, as depicted in Fig. 5f, the device transconductance drops approximately by 30% once vacuum is introduced into the measurement system. The other 6 samples give a similar trend, and the rest of the results are compiled in Table S1 (ESI†). Interestingly, these results are perfectly consistent to those reported by Gao *et al.*,[40] in which the device transconductance difference between InAs NWs measured under air and vacuum conditions can be up to 6 fold. Actually, $InAs_{1-x}Sb_x$, similar to InAs, is known to also have a surface accumulation layer.[41] This layer is mainly composed of a non-stoichiometric oxide film, being extremely sensitive to ambient environment, such as the adsorption of gas molecules onto the surface. In particular, the ambient water vapor molecules would induce significant hysteresis in the device characteristics and simultaneously enhance the mobility by reducing the surface charge density.[40,42] All these findings confirm the existence of a surface charge layer of $InAs_{1-x}Sb_x$ NWs and its role would provide further insights on how to better modify and engineer the NW surface for enhanced functionalities.

Conclusions

In summary, crystalline As-rich $InAs_{1-x}Sb_x$ NWs are successfully grown on amorphous substrates using solid-source chemical vapor deposition. By simply controlling the precursor powder mixing ratio between InAs and InSb, the morphology and composition of NWs can be controlled reliably. It is also noted that the NWs have an unusual phase-pure zinc blende structure, which has not yet been achieved by other works, being a distinct contrast to the typical $InAs_{1-x}Sb_x$ NWs grown with the mixed zinc blende and wurtzite phases. Importantly, when configured into field-effect transistors, the $InAs_{0.948}Sb_{0.050}$ NW devices exhibit a better performance, especially the electron mobility as compared with the pure InAs NW counterparts, which can be attributed to the reduced effective electron mass because of the Sb alloying. On the other hand, the on–off current ratio of the devices deteriorates with the increasing Sb concentration of NWs due to the reduction of bandgap. Moreover, the electrical characteristics of NW devices are found to be sensitive to the measurement environment. The device transconductance has a decrease of approximately 30% for the measurement performed under vacuum, suggesting the existence of a surface charge accumulation layer that is commonly observed in other As-based III–V NWs. The NW surface can be potentially manipulated to further enhance the functionality. All these results indicate the promising potential of these high-quality phase-pure zinc blende $InAs_{1-x}Sb_x$ NWs for high-mobility electronic devices.

Experimental

Nanowire growth

The $InAs_{1-x}Sb_x$ NWs were grown on pre-cleaned Si/SiO_2 wafer pieces, in which a 0.5 nm-thick Au layer was pre-deposited as the catalyst by thermal evaporation. The catalyst-coated substrate was then loaded in the downstream zone of a quartz tube placed in a 2-zone horizontal tube furnace, while the precursor powder mixture of InAs (99.9999% purity) and InSb (99.9999% purity) filled in two separate boron nitride crucibles (1 g + 1 g) is loaded in the upstream zone. The schematic illustration of the entire growth set-up is shown in Fig. S1a (ESI†). When the growth was started, the quartz tube was first pumped down to a vacuum of 1.5×10^{-3} Torr. Ultra-high purity hydrogen gas (99.999%) was fed into the quartz tube as a carrier gas until the

entire growth process was completed. After purging the quartz tube with hydrogen gas for 3 minutes, the substrate zone was heated up to 560 °C. During the temperature ramp-up stage, once the substrate temperature reached 300 °C, the source zone was heated up to 670 °C. The temperature profiles are also presented in Fig. S1b (ESI†). After both the zones reached the target temperatures, the growth system was held for another 45 minutes before it was naturally cooled down to room temperature.

Material characterization

Field-emission scanning electron microscopy (FESEM, FEI/Philips XL30) and transmission electron microscopy (TEM, Philips CM-20) were used to examine the morphologies of the obtained NWs. The chemical composition of the NWs was evaluated using an Energy dispersive X-ray spectrometry (EDS) detector attached in the TEM. The NW crystal structure was studied using X-ray diffraction (XRD, D2 Phaser, Brucker) and high-resolution TEM (JEOL JEM-3000F FEGTEM).

Device fabrication and electrical measurement

The back-gated NW FETs were fabricated on heavily p-doped silicon wafer pieces pre-grown with a 50 nm-thick thermal oxide film. The NWs were first transferred onto the substrate by drop-casting the NW suspension, which was created by the ultra-sonication of the as-grown NW substrate in anhydrous ethanol. The electrode regions were patterned using traditional photolithography, followed by the thermal evaporation of the Ni film (80nm thick) and the lift-off process. The electrical measurement was performed in a standard probe station chamber connected to a dry pump and a molecular pump, where these pumps would be turned on for the measurement under vacuum (5×10^{-6} Torr). A Keysight B1500A semiconductor device analyzer was used to measure the current *versus* voltage characteristics of the NW devices.

Conflicts of interest

There are no conflicts to declare.

Acknowledgements

This work is financially supported by the National Natural Science Foundation of China (Grants 51672229), the General Research Fund (CityU 11211317) and the Theme-based Research (T42-103/16-N) of the Research Grants Council of Hong Kong SAR, China, the Science Technology and Innovation Committee of Shenzhen Municipality (Grant JCYJ20170818095520778) and a grant from the Shenzhen Research Institute, City University of Hong Kong.

Notes and references

1 J. A. Del Alamo, *Nature*, 2011, **479**, 317–323.
2 J. B. Boos, W. Kruppa, B. R. Bennett, D. Park, S. W. Kirchoefer, R. Bass and H. B. Dietrich, *IEEE Trans. Electron Devices*, 1998, **45**, 1869–1875.
3 S. Mokkapati and C. Jagadish, *Mater. Today*, 2009, **12**, 22–32.
4 J.-M. Wun, Y.-W. Wang, Y.-H. Chen, J. E. Bowers and J.-W. Shi, *IEEE Trans. Electron Devices*, 2016, **63**, 2796–2801.
5 Y. Wan, Z. Zhang, R. Chao, J. Norman, D. Jung, C. Shang, Q. Li, M. Kennedy, D. Liang and C. Zhang, *Opt. Express*, 2017, **25**, 27715–27723.
6 H. Liu, T. Wang, Q. Jiang, R. Hogg, F. Tutu, F. Pozzi and A. Seeds, *Nat. Photonics*, 2011, **5**, 416–419.
7 K. Tanabe, D. Guimard, D. Bordel, S. Iwamoto and Y. Arakawa, *Opt. Express*, 2010, **18**, 10604–10608.
8 J. Du, D. Liang, H. Tang and X. P. A. Gao, *Nano Lett.*, 2009, **9**, 4348–4351.
9 P. Offermans, M. Crego-Calama and S. Brongersma, *Nano Lett.*, 2010, **10**, 2412–2415.
10 F. Rothmayr, A. Pfenning, C. Kistner, J. Koeth, G. Knebl, A. Schade, S. Krueger, L. Worschech, F. Hartmann and S. Höfling, *Appl. Phys. Lett.*, 2018, **112**, 161107.
11 A. Westlund, P. Sangaré, G. Ducournau, P.-Å. Nilsson, C. Gaquière, L. Desplanque, X. Wallart and J. Grahn, *Appl. Phys. Lett.*, 2013, **103**, 133504.
12 R. Biefeld and S. Kurtz, *Infrared Detectors and Emitters: Materials and Devices*, Springer, 2001, pp. 205–232.
13 E. Delli, V. Letka, P. D. Hodgson, E. Repiso, J. P. Hayton, A. P. Craig, Q. Lu, R. Beanland, A. Krier and A. R. Marshall, *ACS Photonics*, 2019, **6**, 538–544.
14 W. Dobbelaere, J. De Boeck, C. Bruynserede, R. Mertens and G. Borghs, *Electron. Lett.*, 1993, **29**, 890–891.
15 H. Choi, G. Turner and M. Manfra, *Electron. Lett.*, 1996, **32**, 1296–1297.
16 M. J. Sourribes, I. Isakov, M. Panfilova, H. Liu and P. A. Warburton, *Nano Lett.*, 2014, **14**, 1643–1650.
17 D. Ren, K. M. Azizur-Rahman, Z. Rong, B.-C. Juang, S. Somasundaram, M. Shahili, A. C. Farrell, B. S. Williams and D. L. Huffaker, *Nano Lett.*, 2019, **19**, 2793–2802.
18 J. Svensson, N. Anttu, N. Vainorius, B. M. Borg and L.-E. Wernersson, *Nano Lett.*, 2013, **13**, 1380–1385.
19 J. E. Sestoft, T. Kanne, A. N. Gejl, M. von Soosten, J. S. Yodh, D. Sherman, B. Tarasinski, M. Wimmer, E. Johnson and M. Deng, *Phys. Rev. Mater.*, 2018, **2**, 044202.
20 R. t. Lutchyn, E. Bakkers, L. P. Kouwenhoven, P. Krogstrup, C. Marcus and Y. Oreg, *Nat. Rev. Mater.*, 2018, **3**, 52–68.
21 L. Ma, W. Hu, Q. Zhang, P. Ren, X. Zhuang, H. Zhou, J. Xu, H. Li, Z. Shan and X. Wang, *Nano Lett.*, 2014, **14**, 694–698.
22 D. Li, C. Lan, A. Manikandan, S. Yip, Z. Zhou, X. Liang, L. Shu, Y.-L. Chueh, N. Han and J. C. Ho, *Nat. Commun.*, 2019, **10**, 1–10.
23 T. Xu, K. A. Dick, S. Plissard, T. H. Nguyen, Y. Makoudi, M. Berthe, J.-P. Nys, X. Wallart, B. Grandidier and P. Caroff, *Nanotechnology*, 2012, **23**, 095702.
24 B. M. Borg, K. A. Dick, J. Eymery and L.-E. Wernersson, *Appl. Phys. Lett.*, 2011, **98**, 113104.
25 E. Anyebe, M. K. Rajpalke, T. D. Veal, C. Jin, Z. Wang and Q. Zhuang, *Nano Res.*, 2015, **8**, 1309–1319.
26 J. L. Boland, F. Amaduzzi, S. Sterzl, H. Potts, L. M. Herz, I. M. A. Fontcuberta and M. B. Johnston, *Nano Lett.*, 2018, **18**, 3703–3710.

27 Z.-x. Yang, S. Yip, D. Li, N. Han, G. Dong, X. Liang, L. Shu, T. F. Hung, X. Mo and J. C. Ho, *ACS Nano*, 2015, **9**, 9268–9275.
28 J. J. Hou, N. Han, F. Wang, F. Xiu, S. Yip, A. T. Hui, T. Hung and J. C. Ho, *ACS Nano*, 2012, **6**, 3624–3630.
29 S. Yip, L. Shen and J. C. Ho, *Nanotechnology*, 2019, **30**, 202003.
30 B. M. Borg and L.-E. Wernersson, *Nanotechnology*, 2013, **24**, 202001.
31 W.-N. Du, X.-G. Yang, X.-Y. Wang, H.-Y. Pan, H.-M. Ji, S. Luo, T. Yang and Z.-G. Wang, *J. Cryst. Growth*, 2014, **396**, 33–37.
32 D. Ren, D. L. Dheeraj, C. Jin, J. S. Nilsen, J. Huh, J. F. Reinertsen, A. M. Munshi, A. Gustafsson, A. T. van Helvoort and H. Weman, *Nano Lett.*, 2016, **16**, 1201–1209.
33 D. Ercolani, F. Rossi, A. Li, S. Roddaro, V. Grillo, G. Salviati, F. Beltram and L. Sorba, *Nanotechnology*, 2009, **20**, 505605.
34 D. Ercolani, M. Gemmi, L. Nasi, F. Rossi, M. Pea, A. Li, G. Salviati, F. Beltram and L. Sorba, *Nanotechnology*, 2012, **23**, 115606.
35 L. Namazi, S. G. Ghalamestani, S. Lehmann, R. R. Zamani and K. A. Dick, *Nanotechnology*, 2017, **28**, 165601.
36 S.-Y. Chen, C.-Y. Wang, A. C. Ford, J.-C. Chou, Y.-C. Wang, F.-Y. Wang, J. C. Ho, H.-C. Wang, A. Javey and J.-Y. Gan, *Phys. Chem. Chem. Phys.*, 2013, **15**, 2654–2659.
37 D. Chattopadhyay, S. Sutradhar and B. Nag, *J. Phys. C: Solid State Phys.*, 1981, **14**, 891.
38 S. Adachi, *Properties of semiconductor alloys: group-IV, III–V and II-VI semiconductors*, John Wiley & Sons, 2009.
39 C. Thelander, P. Caroff, S. Plissard and K. A. Dick, *Appl. Phys. Lett.*, 2012, **100**, 232105.
40 J. Du, D. Liang, H. Tang and X. P. Gao, *Nano Lett.*, 2009, **9**, 4348–4351.
41 T. Krug, L. Botha, P. Shamba, T. Baisitse, A. Venter, J. Engelbrecht and J. Botha, *J. Cryst. Growth*, 2007, **298**, 163–167.
42 A. Ullah, H. Joyce, H. Tan, C. Jagadish and A. Micolich, *Nanotechnology*, 2017, **28**, 454001.